Red and NIR light dosimetry in the human deep brain

Article *in* Physics in Medicine & Biology · March 2015

DOI: 10.1088/0031-9155/60/7/2921 · Source: PubMed

7 authors, including:

Andreas Pitzschke
Lausanne University Hospital
36 PUBLICATIONS **536** CITATIONS
SEE PROFILE

Martin Pfleiderer
Dentsply Sirona
13 PUBLICATIONS **324** CITATIONS
SEE PROFILE

Georges A Wagnières
Swiss Federal Institute of Technology in Lausanne
290 PUBLICATIONS **8,611** CITATIONS
SEE PROFILE

IOP Publishing | Institute of Physics and Engineering in Medicine Physics in Medicine & Biology

Phys. Med. Biol. **60** (2015) 2921–2937 doi:10.1088/0031-9155/60/7/2921

Red and NIR light dosimetry in the human deep brain

A Pitzschke[1], B Lovisa[1,2], O Seydoux[1], M Zellweger[1], M Pfleiderer[2], Y Tardy[2] and G Wagnières[1]

[1] Federal Institute of Technology (EPFL), Institute of Chemical Sciences and Engineering (ISIC), 1015 Lausanne, Switzerland
[2] Medos International Sàrl, Chemin Blanc 38, 2400 Le Locle, Switzerland

E-mail: andreas.pitzschke@chuv.ch and georges.wagnieres@epfl.ch

Received 6 August 2014, revised 24 January 2015
Accepted for publication 12 February 2015
Published 19 March 2015

Abstract

Photobiomodulation (PBM) appears promising to treat the hallmarks of Parkinson's Disease (PD) in cellular or animal models. We measured light propagation in different areas of PD-relevant deep brain tissue during transcranial, transsphenoidal illumination (at 671 and 808 nm) of a cadaver head and modeled optical parameters of human brain tissue using Monte-Carlo simulations. Gray matter, white matter, cerebrospinal fluid, ventricles, thalamus, pons, cerebellum and skull bone were processed into a mesh of the skull (158 × 201 × 211 voxels; voxel side length: 1 mm). Optical parameters were optimized from simulated and measured fluence rate distributions. The estimated μ_{eff} for the different tissues was in all cases larger at 671 than at 808 nm, making latter a better choice for light delivery in the deep brain. Absolute values were comparable to those found in the literature or slightly smaller. The effective attenuation in the ventricles was considerably larger than literature values. Optimization yields a new set of optical parameters better reproducing the experimental data. A combination of PBM via the sphenoid sinus and oral cavity could be beneficial. A 20-fold higher efficiency of light delivery to the deep brain was achieved with ventricular instead of transcranial illumination. Our study demonstrates that it is possible to illuminate deep brain tissues transcranially, transsphenoidally and via different application routes. This opens therapeutic options for sufferers of PD or other cerebral diseases necessitating light therapy.

Keywords: light dosimetry, tissue optics, NIR, brain, photobiomodulation, Parkinson, substantia nigra

(Some figures may appear in colour only in the online journal)

1. Introduction

Parkinson's Disease (PD) is a common neurodegenerative disorder of middle-aged and elderly people, affecting 1.8% of individuals over 65 (Morais and De Strooper 2010) and up to 4% of the population over 80 (Davie 2008, Lees *et al* 2009). The pathological hallmark of PD is the loss of dopaminergic neurons from the pars compacta of the brain's substantia nigra (SNpc) (McNaught and Jenner 2001, Samii *et al* 2004, Davie 2008, Lees *et al* 2009), although cell loss in other structures of the brain is also reported (Damier *et al* 1999). The cell loss is accompanied by other features, such as intraneuronal inclusions made of abnormal, aggregated forms of the protein α-synuclein called Lewy bodies (McNaught and Jenner 2001, Kordower *et al* 2008, Lees *et al* 2009, Morais and De Strooper 2010) and breakdown of mitochondrial metabolism and functionality (Lees *et al* 2009, Trimmer *et al* 2009, Morais and De Strooper 2010). Whilst PD is an incurable disease, treatments improve quality of life and functional capabilities of patients. Treatment approaches include oral, injected or enteric administered drugs, but are often associated with side effects (Davie 2008, Lees *et al* 2009). Other treatment options have been explored but have yet to find their way into the mainstream treatment of PD (fetal tissue transplantation) or have been abandoned (surgery) (Samii *et al* 2004, Temel *et al* 2006, Davie 2008, Lees *et al* 2009). Deep-brain stimulation is now widely accepted for selected patients that are no longer responsive to drug treatment, yet only symptoms can be treated. To this day, there is no therapeutic option that brings neuroprotection or neuroregeneration to patients, although some promising results are reported on animal models (Shaw *et al* 2010, Shaw *et al* 2012). Photobiomodulation (PBM) has been described to bring positive results by restoring mitochondrial functionality in metabolically and functionally compromised PD tissue cell lines (Hamblin and Demidova 2006, Trimmer *et al* 2009) and in animal models such as the Drosophila (Vos *et al* 2013) or mouse (Shaw *et al* 2010). The hypothesized mechanism is that the red/NIR-light photostimulation of the diseased tissue improves the electron transport chain function and restores some functional activity of mitochondria, leading to the restoration of locomotor functions in the animal models (Moro *et al* 2013, Vos *et al* 2013).

The objective of the present study was to explore experimentally the light delivery and dosimetry for a transcranial, transsphenoidal photostimulation of the SNpc as a possible treatment option for PD patients. We wanted to evaluate how the sphenoid sinus (S.S.) can be accessed with a light diffuser and how it can be positioned and oriented towards the SNpc, if necessary with the help of an endoscope. This allowed to quantify the light distribution within brain tissue when illuminating from the nasal cavity and to define the best treatment regimes with a controlled energy deposition. Since light dosimetry depends, among others, on the tissue optical properties, we had to model the intracranial fluence rate distribution by Monte Carlo simulations based on the real patient skull mesh. An iterative algorithm lead to a self-consistent set of optical parameters for the model's tissues. The model was validated by directly measuring the fluence rate distribution in selected intracranial locations of a human cadaveric head, from the dura mater just behind the S.S., the pituitary gland, to the most posterior-inferior area of the treatment target, the SNpc. Furthermore, our self-consistent model enabled us to explore the light delivery to the SNpc using an interventricular/interstitial approach. The wavelengths of 671 and 808 nm chosen in our study correspond to the maxima in the action spectrum of cytochrome *c* oxidase, which is the terminal enzyme of the respiratory chain driving the ATP production in the mitochondria (Karu 1999). The results of this work shall provide useful information to determine whether it is feasible to deliver sufficient illumination power to the relevant brain area to induce a therapeutic effect, whilst preserving

the structures located between light diffuser and target area. It sheds light onto the exact power density that reaches specific brain regions.

2. Materials and methods

2.1. Measurement of the fluence rate distribution

2.1.1. Human cadaver. The measurement of the fluence rate distribution was carried out on a human cadaveric head (56 years, female, 61 kg, primary cause of death: chronic obstructive pulmonary disease, head dissected from the torso between the 3rd and 4th cervical vertebra) with no sign of head injury. The specimen was purchased from Innoved Institute, LLC (Bensenville, IL, USA). The supplier kept the specimen refrigerated at 4 °C post-mortem for 4 d and then frozen for 20 months at −20 °C prior to the delivery. No additional antifreeze agent or perfusion was applied.

Prior to MRI scan at the supplier facility, the specimen was taken from the fridge and kept at 4 °C during 4 d. 10 h before the scan, the specimen was left at ambient room temperature to ensure thaw. Immediately after imaging, the specimen was placed back into the freezer at −20 °C and then distributed to the measurement lab on dry ice. Upon delivery, the specimen was kept in the fridge at 8 °C for one day to ensure full thaw. Titanium bone screws (4 × 1.5 mm, Bioplate, Los Angeles, CA) were fixed to the skull prior to the CT scan and optical measurements to serve as reference positions for registration of the head coordinates. A CT scan was carried out the day before the optical measurement at the measurement lab. The specimen was placed back in the fridge at 8 °C overnight prior to the optical measurements. The coregistration of MRI and CT image datasets followed standard protocols of Brainlab's planning and navigation software (Navigation System Kolibri 2.0, Navigation Software Cranial 2.1 and Planning Software iPlan RT, Brainlab AG, Feldkirchen b. M., Germany).

The measurements were carried out at ambient temperature; no further MRI or CT scans were performed after the optical measurements. Soft tissue geometry was assumed to be unaltered between CT/MRI scans and optical measurements. A rigid coordinate transformation was used, which could result in some minor positioning uncertainties due to tissue displacement.

2.1.2. Light diffuser and isotropic probes for in situ fluence rate measurements. The red and NIR light was delivered by an optical fiber-based frontal light diffuser (FD1, Medlight SA, Ecublens, Switzerland) introduced into the nasal cavity. This light distributor emitted light in a cone shape (full aperture angle 34.7 degree in the VIS/NIR wavelength range) towards the SNpc. The FD1 was coupled to a laser diode at 671 nm (FSDL-671, Frankfurter Laser, Friedrichshof, Germany) or 808 nm (RLTMDL-808-5W, 5W, Roithner Lasertechnik GmbH, Vienna, Austria).

Optical fiber-based isotropic probes (IP85, Medlight SA, Switzerland) with a diameter of 0.85 mm were used to measure *in situ* the fluence rate along the trajectories of five catheters (iCAT-2.0-200, OD 2 mm, Medlight SA, Ecublens, Switzerland), which were inserted at five positions into the deep brain (figure 1). The influence of the catheter on the fluence rate measurements, i.e. light attenuation and waveguide effects, was determined by illuminating the isotropic probes with and without the catheter in an integrating sphere (LMS-200, 20 inch diameter, Labsphere, Inc., USA) or directly with a calibrated collimated light beam at 671 and 808 nm. The changes in the measured fluence rate due to the presence of a catheter were smaller than 5%. Only at the catheter tip probe shading became prominent, such that experimental data acquired close to the tip (usually for probe-tip distances below 3 mm) were

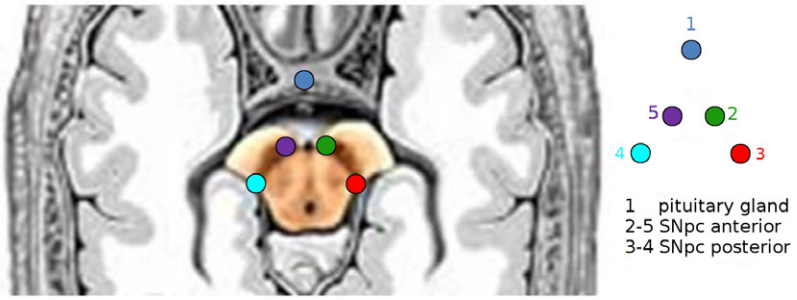

Figure 1. Transaxial view at the level of the SNpc with the catheters placed into the pituitary gland, anterior and posterior SNpc. The SNpc is colorized in brown.

excluded from data analysis. The isotropic probes were coupled to a calibrated multi-channel optical power meter (OP710-IN, OptoTest Corporation, Camarillo, CA, USA).

2.1.3. Protocol for the ex vivo measurement of the intracranial fluence rate distribution. The position of the SNpc was determined on the pre-op MRI by identifying the Red Nucleus, to which the SNpc is situated lateral and anterior. The five target positions (SNpc right posterior, right anterior, left posterior, left anterior and pituitary gland, see figure 1) on the MRI were taken as input for the planning software. The skull entry points on the frontal lobe were selected with the help of the navigation system in such a way that the five catheters were orthogonal to the FD1 in the sagittal view as well as parallel to one another. Five burr holes were drilled in the skull at the entry positions and the five catheters (modified to a length of 160 mm, Brainlab stylet with 1.1 mm diameter) were guided by the navigation system to a depth in the brain that surpassed the four target points of the SNpc by approximately 5 mm. The catheter into the pituitary gland was guided down to the sellaturcica in contact with the sphenoidal bone. The catheters in the SNpc were found to be within 2 mm of the target location selected on the pre-op MRI. The position of the catheter in the pituitary gland was confirmed by fluoroscopy.

In the sphenoidal sinus (S.S.), the placement of the light diffuser was carried out under endoscopy and fluoroscopy. The resulting location and orientation of the diffuser, guided by a 10 mm long steel tube (Relieva Sinus Guide Catheter, Acclarent, Menlo Park, CA, USA), were controlled and documented by the navigation software. The S.S. was prepared by inserting a balloon sinuplasty system (Relieva, Acclarent, Menlo Park, CA, USA) and resecting the septum between the left and right S.S. After irrigation and suction to clear the sphenoidal cavity of remaining ice and mucus, a sinus catheter (Relieva Sinus Guide Catheter, Acclarent, Menlo Park, CA, USA) was inserted into the S.S. and positioned right after the ostium, thereby keeping a distance of 15–20 mm from the posterior sinus mucosa. The FD1 was introduced through the sinus catheter with its tip just surpassing the tip of the catheter, such that it produced a circular homogenous light spot of approximately 1 cm^2 on the sinus mucosa. For alignment and calibration purposes of the FD1, the light of a green laser pointer was injected into the fiber and its spot position on the posterior wall was verified endoscopically with the help of a rigid rhinoscope. The laser power from the FD1 was set to 1 W at 808 nm and to 0.8 W at 671 nm (maximum output power of the laser diode) with the help of a power meter (detector 818P-010-12, driver 1918-R, Spectra Physics Newport). The five isotropic probes were inserted into the catheters and the background signal was measured with the laser switched off. With laser on, measurements were performed by withdrawing synchronously each probe inside the catheters in nine steps of 5 mm each with the starting point on the catheters' distal

end. The measurement sequence was repeated five times to assess typical fluence rate variations for each measurement.

2.2. Modeling of the light propagation

2.2.1. Analytical model based on the diffusion approximation. Many analytical models describing the propagation of light in biological tissue are based on the diffusion approximation. The steady-state expression of the photon diffusion within a homogenous medium (Ishimaru 1978) is given by

$$(\nabla^2 - \mu_{\text{eff}}^2)\phi(\mathbf{r}) = -q(\mathbf{r})/D, \tag{1}$$

where ϕ ($\mathbf{r}$) is the fluence rate (mW cm^{-2}), $\mu_{\text{eff}} = [3\mu_a(\mu_a + \mu_s(1-g))]^{1/2}$ the effective attenuation coefficient (cm^{-1}), $D = \mu_a/\mu_{\text{eff}}^2$ the optical diffusivity (cm) and q the diffusive photon density (mW cm^{-3}). The absorption and scattering coefficients, μ_a (cm^{-1}) and μ_s (cm^{-1}), express the probability for a photon to be absorbed or scattered on a given path length. Analytical solutions of equation (1) for point, line and plane sources can be found in the literature (Tromberg *et al* 1996, Jacques 1998).

Radiation in the visible and near-visible range is normally subject to anisotropic scattering in tissue, which is the result of inhomogeneities of the refractive index. The Henyey–Greenstein phase function (Henyey and Greenstein 1941) is frequently used to model the scattering angle probability density function and is given by

$$p(\theta) = \frac{1 - g^2}{4\pi(1 + g^2 - 2g\cos\theta)^{3/2}}, \tag{2}$$

where g is the anisotropy factor. It is equal to the mean cosine of the scattering angle θ and ranges from −1, total back scattering, over 0, isotropic (Rayleigh) scattering, to +1, total forward scattering (Mie scattering at large particles). In the diffusion theory, the anisotropic scattering is simplified to the isotropic case by defining the reduced scattering coefficient $\mu_s' = \mu_s(1-g)$ (cm^{-1}).

This analytical model is in general accurate if $\mu_a \ll \mu_s'$ and if the light distribution is studied far enough from the light distributor and boundaries, typically at a distance much larger than $1/\mu_s'$. The model becomes unwieldy in complex geometries, e.g. a human skull with different tissue types or more complex light source geometries. In these more complicated cases, remedy can be found in using numerical approaches, e.g. Monte Carlo methods.

2.2.2. Monte Carlo model of the fluence rate. Monte Carlo methods involve a broad class of computational algorithms that rely on repeated random sampling to obtain numerical results (Wang *et al* 1995, Wang and Wu 2007, Zhu and Liu 2013). They are most suited when it is impossible to obtain a closed-form expression of the fluence rate or when deterministic algorithms cannot be applied. Nowadays algorithms are capable to efficiently simulate complex geometries and source emission patterns, boundary conditions, local changes in the refractive index and optical parameters. In this study, the Monte Carlo algorithm MCX (Fang and Boas 2009a), accelerated by graphics processing units, was used to model the photon migration in 3D. The code is implemented with NVIDIA CUDA programming and was validated, with the 3D skull model, against MMC (Fang 2010) and TracePro (Lambda Research Corporation, Littletown, MA, USA). The codes were run on an Intel i7-3930K, 32 GB RAM and a NVIDIA GTX 670 graphics card with 2 GB RAM.

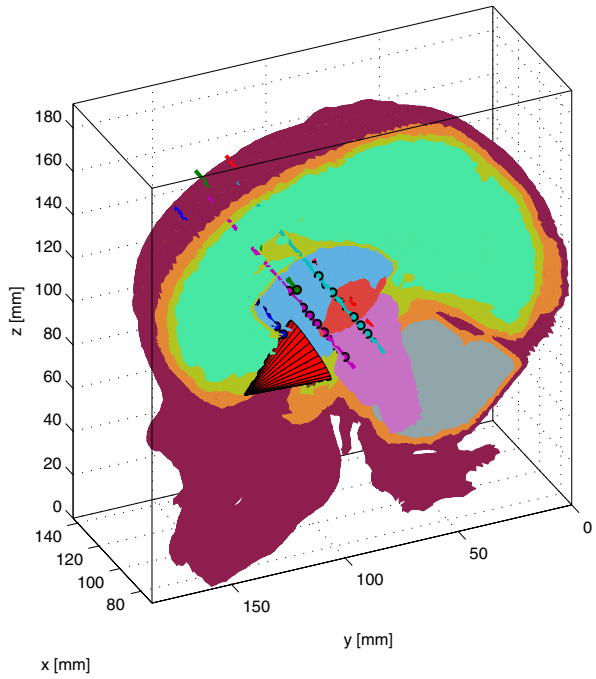

Figure 2. View on the 3D mesh of the skull. The frontal light distributor (located at the origin of the red cone) placed in the nasal cavity is illuminating the SNpc through bone (∼ 2 mm, dark mauve), CSF (∼ 2 mm, orange), gray matter (∼ 2 mm, light green), white matter (∼ 7 mm, dark green) and brainstem (∼ 4–18 mm, light mauve) tissue. The thalamus is depicted in red, the cerebellum in gray. The catheters are shown as colored trajectories with circular marks representing the individual positions of the isotropic probes during the measurement. The catheter color coding is identical with the one used in figure 1.

The optimal number of photons for a simulation with MCX was determined from a statistical noise analysis. For that purpose, a semi-inifinite cube (side length 20 cm, optical coefficients for the human pons (Yaroslavsky *et al* 2002): $\mu_a = 0.6$ cm^{-1}, $\mu_s = 80$ cm^{-1}, $g = 0.92$, $n = 1.37$ refractive-index-matched) was illuminated by an FD1. The algorithm computed the fluence rate distribution in the cube as function of the photon number. For every number of photons, ten computations were carried out, each initialized by a different random prime number to vary the series of random numbers used to compute photon trajectories and absorption events. Photons with relative energy below 10^{-3} of the initial energy were truncated (Cassidy *et al* 2013). In figure 3, the relative statistical error in the fluence rate, $\delta\phi/\langle\phi\rangle$, is shown as function of the number of photons and distance between source and detector, where $\delta\phi$ expresses the standard deviation of the fluence rate. The results indicate that the relative error in the fluence rate becomes minimal beyond a number of 10^9 photons even for the longest distances between source and isotropic probes in the experiment, i.e. 50–60 mm. Therefore, 10^9 photons were chosen for all simulations as a good compromise between accuracy and computational time.

The 3D model of the head was assembled from the MRI and CT reconstruction (see figure 2). In our model, only gray and white matter (GM & WM), cerebrospinal fluid (CSF), ventricles (CSF), thalamus, pons, cerebellum and skull bone were considered. These geometries were then processed with the help of the *iso2mesh* toolbox (Fang and Boas 2009b) to produce a

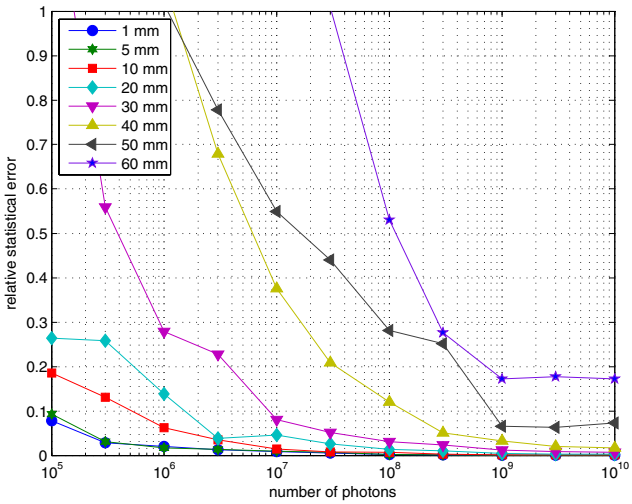

Figure 3. Relative error in the fluence rate, $\delta\phi/\langle\phi\rangle$, at different distances between source and SNpc as function of the number of photons. $\delta\phi$ expresses the standard deviation of the fluence rate ϕ. The relative error was computed by MCX from ten iterations.

tetrahedral and cubic mesh for MCX, MMC and TracePro for cross-verification purposes. The resulting cubic mesh of the skull had a size of 158 × 201 × 211 voxels with a voxel side length of 1 mm. The tetrahedral mesh consisted of around half a million tetrahedra with a distribution of volumes ranging between 1–30 mm^3 and a mean around 13 mm^3. For the eight tissues mentioned above, optical parameters, i.e. the scattering coefficient μ_s, the absorption coefficient μ_a, the refractive index n and the anisotropy factor g, all dependent on the wavelength, were taken from literature (Firbank *et al* 1993, Bevilacqua *et al* 1999, Yaroslavsky *et al* 2002, Koyama *et al* 2005, Custo *et al* 2006).

2.3. Determination of the optical parameters

'*Ab initio*' computations of the intracranial fluence rate distribution with optical parameters from literature showed significant differences from what was measured experimentally (see below in section 3). These differences were attributed to various uncertainties in our model: (1) The optical tissue coefficients for this specimen were unknown, thus initial coefficients had to be taken from literature. However, these values might be inappropriate when one considers their large uncertainties reported in literature (Roggan 1997, Tuchin 2007). (2) Furthermore, tissue storage including freezing and thawing procedures is known to alter optical parameters (Roggan *et al* 1999, Salomatina and Yaroslavsky 2008, Pitzschke *et al* 2015) making it unlikely to match the fluence rate from an '*ab initio*' calculation with the measurements. (3) The positions of the isotropic probes in the catheters during the measurements were only exact to 1–2 mm. Since the fluence rate decays approximately exponentially as function of the distance between source and detector position, small uncertainties in local positioning lead to non-negligible errors in the fluence rate. (4) The mesh construction is, in general, only precise to a certain extent. The identification of different tissue types on gray scale MRI images, reconstruction of 3D meshes, smoothing procedures etc yield a skull model, whose geometric precision was not better than a few millimeters. (5) The computation of the fluence rate based on the statistical Monte Carlo approach has itself uncertainties increasing drastically with the

dimensions of the modeled system (see figure 3). The error sources (1), (2) and (4) are of systematic nature and were corrected for, (3) and (5) are uncorrectable random errors.

To remedy this situation, the optical parameters were derived from a χ^2-iteration procedure optimizing the match between simulated and measured fluence rate distribution. For this purpose, the reduced χ^2-distribution function,

$$\chi^2_{\mathrm{red}} = \frac{1}{\nu} \sum_i \Big[\ln\left(\phi_{\mathrm{sim}}(\mathbf{r}_i, \mu_a, \mu_s{}')\right) - \ln\left(\phi_{\mathrm{exp}}(\mathbf{r}_i)\right) \Big]^2, \tag{3}$$

was minimized for sets of μ_a and μ'_s, where ν is the degree of freedom, $\phi(\mathbf{r})$ the simulated and experimental fluence rate at position $\mathbf{r}$. The natural logarithm of the fluence rate was taken to impose a parabolic behavior in χ^2_{red} and to avoid that small fluence rates, measured far away from the source, are under-weighted. This approach is equivalent to fit directly the optical parameters instead of the fluence rate, since $\mu_{\mathrm{eff}}(\mu_a, \mu'_s) \propto \ln(\phi)$. The minimization algorithm was based on the Levenberg-Marquardt-method, which is implemented in MATLAB's built-in function *lsqnonlin* (R2013a, The MathWorks, Inc., Natick, MA, USA).

Several simplifications of the model were needed to ensure a better convergence of the fitting procedure: (1) The scattering anisotropy was kept constant at $g = 0.9$, which may lead to a bias in μ_s, but keeps μ'_s approximately constant over a wide range of g and μ_s. (2) The refractive indices were set to $n = 1.37$ for tissue and bone and to $n = 1$ for air. (3) The cerebellum was modeled together with the white matter as a single tissue, since no experimental measurements of the fluence rate were carried out in this region of the brain. The optical coefficients of white matter come closest to what is known for the cerebellum (Yaroslavsky *et al* 2002, Tuchin 2007). (4) CSF and ventricles were modeled as a single tissue. (5) Upper and lower boundaries of μ_a and μ'_s, derived from the optical coefficients' minimal and maximal values found in literature (Roggan 1997, Yaroslavsky *et al* 2002, Custo *et al* 2006, Tuchin 2007), were set to constrain the fit.

These simplifications allowed to reduce the number of free parameters from 16 to 12, i.e. six tissues each with a set of μ_a and μ'_s. Thus, 13 simulations per iteration were necessary to compute fluence rate distribution and its derivative as function of the optical parameters. For each iteration, the random number generator of MCX was initialized with the same prime number, such that photon trajectories and absorption as well as absolute values of fluence rate and its derivatives were not subject to statistical noise. Photons with a remaining energy below 10^{-3} of the initial value were truncated. The initial step-size in the relative change of the optical parameters was chosen to be 10% to obtain sensibility of the fitting algorithm on each parameter. Iterations were stopped when either the relative change of χ^2_{red} or the relative change in the optical parameters were below 1% ; mainly the latter condition was reached first. Several starting points with different optical parameters in the range of ± 300% with respect of the literature values presented in table 2 were chosen to ensure global convergence of the fitting algorithm. Usually around ten iterations were sufficient to obtain convergence and reasonable optical parameters.

3. Results and discussion

3.1. Measured fluence rate distribution

The effective attenuation coefficient μ_{eff} was computed from the fluence rate measured by the isotropic probes in the catheter couples anterior-posterior, i.e. 2–3 and 5–4 (see figure 1). The relation

Table 1. The effective attenuation coefficient $\mu_{\text{eff}}^{\text{exp}}$ and its standard deviation (2 SD) in parentheses at 671 and 808 nm was obtained from the fluence rate measurements at the individual positions z (mm) of the isotropic probes in the catheter.

Position z (mm)	Tissue	671 nm		808 nm	
		$\mu_{\text{eff}}^{\text{exp}}$ (cm^{-1})	$\mu_{\text{eff}}^{\text{lit}}$ (cm^{-1})	$\mu_{\text{eff}}^{\text{exp}}$ (cm^{-1})	$\mu_{\text{eff}}^{\text{lit}}$ (cm^{-1})
0	Pons*	4.3 (1.5)	3.5	2.4 (1.1)	3.6
5	Pons/ thal.*	3.6 (1.8)	—	2.3 (0.6)	—
10–20	Thal.	3.4 (0.1)	5.0	2.0 (1.0)	6.0
25	Thal./ ventr.	2.1 (2.5)	—	1.5 (1.0)	—
30–40	Ventr.	1.7 (0.9)	—	1.1 (0.6)	0.5(0.4)

Note: Literature values of $\mu_{\text{eff}}^{\text{lit}}$ for pons and thalamus are taken from Yaroslavsky *et al* (2002), for ventricles (CSF) in the NIR from Koyama *et al* (2005). Slash characters indicate the transition from one tissue to another around a measurement position. The asterisks indicate positions were the SNpc was assumed to be located.

$$\phi_i(z) \simeq \phi_j(z)\mathrm{e}^{-\mu_{\text{eff}}(z)d_{ij}} \tag{4}$$

was used to compute $\mu_{\text{eff}}(z)$, where $\phi_i(z)$ and $\phi_j(z)$ are the fluence rates in different catheters (i, j, $i \neq j$) at a position z of the isotropic probes in the catheter and d_{ij} the distances between the measurement positions. The resulting μ_{eff} for the different tissues and wavelengths are presented in table 1 together with typical values from literature.

Equation (4) is a solution of equation (1) that assumes a planar light source and an infinite homogenous medium, which does not exactly correspond to our case. Far from the source, however, the distance dependence of ϕ is essentially mono-exponential, as has been shown elsewhere (Bays *et al* 1997, Jacques 1998). Monte Carlo simulations showed fluence rate contours in brainstem and thalamus to be approximately parallel to the catheter trajectories (figure 6(*a*)), thus validating above taken approximation.

The estimated μ_{eff} for the different tissues was, despite the large uncertainties, in all cases larger at 671 as compared to 808 nm. Absolute values were comparable to those found in literature or slightly smaller, which may be the effect of storing, freezing and thawing or a drain of liquids from the cadaveric head during the preparation and measurement procedures. The freezing process, especially when performed slowly, is supposed to partially damage cell membranes leading to changes of the optical parameters (Roggan *et al* 1999, Salomatina and Yaroslavsky 2008). However, blood drain was shown to have only little effect on the attenuation coefficient of brain tissue (Pitzschke *et al* 2015). The effective attenuation in the ventricles was considerably larger as compared to literature values (Koyama *et al* 2005). This discrepancy might be due to impurities in the CSF like debris from tissue degeneration or contamination by blood from the Arteria pericallosa or other surrounding blood vessels that were damaged by repeated freeze and thaw of the head. Furthermore, the head resection may have lead to leaking of CSF emptying the ventricles to some extent. On the MRI data (not shown here), a partial collapse of the left ventricle was visible, which would explain a somewhat larger μ_{eff} for the ventricles.

3.2. Determination of the optical parameters by Monte Carlo simulations

The computation of the fluence rate distribution was carried out with a straightforward Monte Carlo simulation using the tissue optical parameters from the literature (table 2), which were

Table 2. The optical coefficients, μ_a, μ_s' and μ_{eff}, fitting best the fluence rate measurements at 671 and 808 nm.

	671 nm			808 nm			Literature values for 671–808 nm		
Tissue	μ_a (cm^{-1})	μ_s' (cm^{-1})	μ_{eff} (cm^{-1})	μ_a (cm^{-1})	μ_s' (cm^{-1})	μ_{eff} (cm^{-1})	μ_a (cm^{-1})	μ_s' (cm^{-1})	μ_{eff} (cm^{-1})
Skull	0.07 (0.17)	12.7 (1.3)	1.6 (2.6)	0.04 (0.17)	5.4 (1.1)	0.8 (2.6)	0.19–0.50	8.6–17	2.2–5.1
CSF	0.15 (0.04)	11.6 (1.2)	2.3 (0.4)	0.05 (0.02)	5.9 (1.6)	1.0 (0.4)	0.04–0.14	0.1–0.3	0.1–0.4
GM	0.08 (0.17)	7.1 (0.9)	1.4 (2.0)	0.06 (0.18)	5.4 (1.2)	1.0 (2.0)	0.20–0.36	7.0–8.4	2.1–3.1
WM	0.27 (0.26)	27.8 (4.6)	4.8 (3.3)	0.31 (0.36)	20.4 (4.6)	4.4 (3.3)	0.70–1.00	41.0–60.0	9.4–13.5
Pons	0.68 (0.31)	3.7 (0.5)	3.0 (1.0)	0.51 (0.22)	3.6 (0.9)	2.5 (1.0)	0.60–0.80	6.4–8.6	3.5–4.7
Thal.	0.68 (0.17)	5.1 (0.8)	3.4 (0.7)	0.23 (0.06)	5.4 (1.5)	2.0 (0.7)	0.44–0.65	17.6–19.0	4.9–6.2

Note: Values in parenthesis correspond to the parameter uncertainties (2 SD). The coefficients derived from literature (Firbank *et al* 1993, Bevilacqua *et al* 1999, Yaroslavsky *et al* 2002, Koyama *et al* 2005, Custo *et al* 2006) for the red/NIR-range are given in the last column.

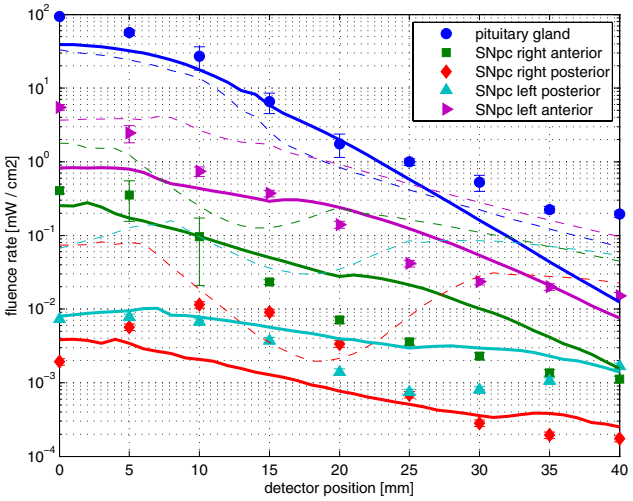

(a)

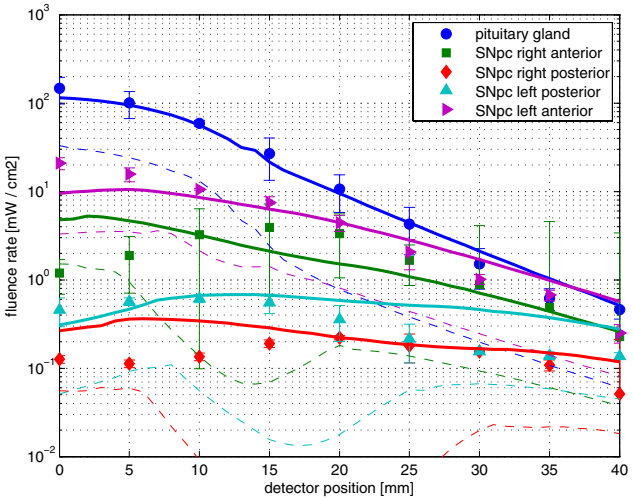

(b)

Figure 4. The fluence rate (mW cm^{-2}) at different detector positions (markers with errorbars (2 SD)) and for the calculated optical parameters (solid line) is shown in figures 4(*a*) and (*b*) for 671 and 808 nm, respectively. Dashed lines represent the fluence rate computed with optical parameters derived from literature (table 2). The zero-position on the *x*-axis corresponds to the caudal limit of the SNpc. Experimental and simulated data was normalized such that the tissue irradiance of the conic beam delivered by the FD1 on the sphenoidal bone was 1 W cm^{-2}. (*a*) Fluence rate at 671 nm. (*b*) Fluence rate at 808 nm.

chosen for their completeness in wavelengths and tissue types. Figures 4(*a*) and (*b*) show the simulation results for 671 and 808 nm as dashed lines together with the experimental data as markers. For both wavelengths, simulation results using optical parameters derived from the literature fit only poorly the experimental data. In certain conditions the simulated fluence rate showed deviations by one order of magnitude from the experimental one. We could exclude these deviations that were only due to an imperfect mesh construction. Although

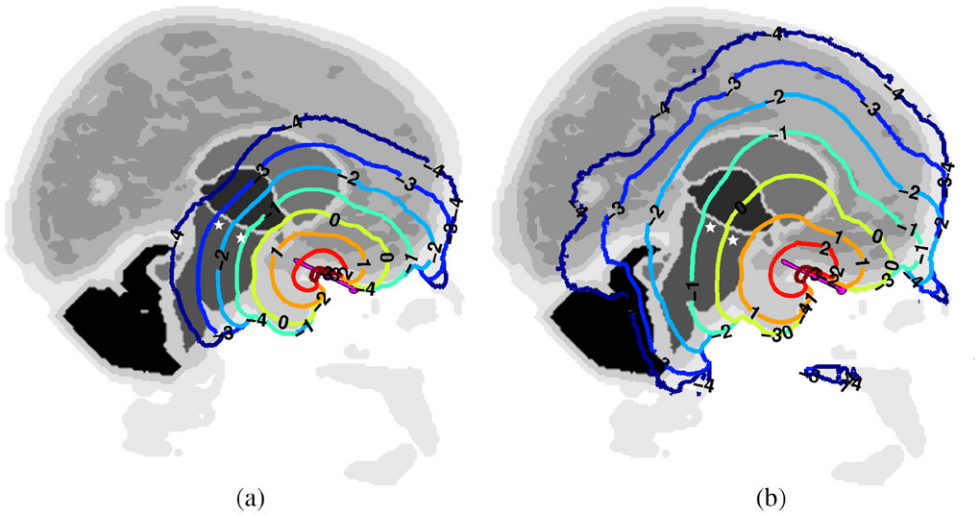

Figure 5. Colored contours of the $\log_{10}$ fluence rate (mW cm^{-2}) computed from the determined optical parameters are indicated in figures 5(*a*) and (*b*) for 671 and 808 nm, respectively. The sagittal plane of the skull is shown in gray-scale, the orientation of the FD1 indicated in magenta and the anterior/posterior location of the SNpc as white asterisks. Contour lines of experimental and simulated data was normalized such that the tissue irradiance of the conic beam delivered by the FD1 on the sphenoidal bone was 1 W cm^{-2}. (*a*) Fluence rate distribution at 671 nm. (*b*) Fluence rate distribution at 808 nm.

absolute values of the fluence rate might be biased by the mesh, large local over- or underestimation of the fluence rate is rather an indication of an inappropriate choice of optical tissue coefficients. The simulated fluence rate showed dip behavior in the region of the thalamus (at the positions around 15 mm for catheters located in the SNpc), in contrast to the experimental data, suggesting a much lower μ_{eff} for this region. The simulated fluence rate in the ventricles (at positions above 30 mm) was approximately the same for all catheter positions, which corresponds to a light cavity with small μ_{eff} and thus semi-homogenous fluence rate distribution. In contrast, the experimental data showed much larger differences in the fluence rate between particular catheters, especially at 671 nm, which suggests a larger μ_{eff} for the CSF in the ventricles. This is consistent with the determined attenuation coefficients in section 3.1, table 1. In other words, the ventricles contained a medium with more scattering and absorbing centers than is usually the case for CSF.

The χ^2-optimization of the optical parameters (section 2.3) yield a new set of optical parameters leading to a better match of simulated and measured data. The simulated fluence rate is shown as solid lines in figures 4(*a*) and (*b*). Deviations of simulated fluence rate in thalamus and ventricles from the experimental data were now much smaller. Nevertheless, these simulation results could not perfectly reproduce the experimental data, which may be due to the simplicity of the brain model as well as an incomplete or missing set of experimental data for cerebellum, gray and white matter and for the CSF in the subarachnoid space. The values of optical tissue parameters derived from the χ^2-optimization are given in table 2 for both wavelengths. As already noted in section 3.1, there was a tendency of decreasing value of μ_{eff} for increasing wavelength leading to a higher light penetration depth in the brain tissue at 808 than at 671 nm (figures 5(*a*) and (*b*)). Both, μ_{a} and μ_{s}' were smaller than cited in the literature, apart from the CSF, which we attributed to be an effect of the freezing and thawing procedures

(Roggan *et al* 1999, Pitzschke *et al* 2015). The higher value of μ_s' for the CSF may result from the ventricles partially collapsed and/or filled by a medium with higher μ_{eff} as noted above.

The standard deviation of the optical tissue parameters presented in table 2 were relatively large for certain values of μ_a, notably for skull, gray and white matter tissue. In these cases, the hyper-surface of the χ^2-function became relatively flat, so that a change in a particular coefficient affected only little the χ^2-cost-function. In other words, since experimental data was partially missing for these tissues, the model was less sensitive to the corresponding optical parameters and, as a consequence, yield larger uncertainties for certain coefficients. In a future study, this issue should be assessed by fluence rate measurements performed more thoroughly in all considered tissues.

As far as the penetration of light to target the SNpc is concerned, the results obtained from the specimen suggest that light at 808 nm is the better choice. This is due to less absorption and reduced scattering at 808 nm in all considered tissue types. Especially when delivering light by the S.S., the reduced light attenuation in thalamus and pons at this wavelength is improving the fraction of fluence rate delivered in the SNpc. Furthermore, lower absorption coefficients lead to lower power deposition within the brain tissue as for 671 nm, making it easier to stay below hyperthermia thresholds. However, for choosing an appropriate wavelength for PBM, the action spectrum must also be taken into account.

3.3. Modeled fluence rate distribution for alternative light delivery routes

To date, there have been no major clinical trials on the therapeutic effect of red/NIR light in patients with PD (Lapchak 2012). One potential problem associated with this treatment relates to the effective and reliable penetration of red/NIR light through the human cranium, meningeal layers and brain parenchyma to reach the SNpc in the midbrain. Similar issues occur in studies for treating strokes (Lapchak and Taboada 2010, Sharma *et al* 2011) or Alzheimer (De Taboada *et al* 2011) by PBM. The lack of precise light dosimetry therefore demands the evaluation of various light delivery routes for their feasibility and efficiency. In the following we present two illustrative examples of our model to evaluate potential light delivery routes.

3.3.1. Illumination of the SNpc by a light diffuser positioned in the oral cavity. A reduction of severe Parkinsonian signs was reported for one patient, who underwent light exposure for a dental treatment (Burchman 2011). The patient received light at 660 nm in the oral cavity for a root canal treatment as well as on the acupuncture point Gallbladder GB#20, situated at the junction of occipital and nuchal regions (Atlas of acupuncture points 2007), to calm the patient's tremors. No information was given about the laser power used for the dental treatment.

We modeled the fluence rate distribution corresponding to this case with an FD1 located in the oral cavity pointing towards the SNpc. The output power of the FD1 was chosen such that the tissue irradiance was 1 W cm^{-2}. The result, shown in figure 6(*a*) for the derived cadaver's optical coefficients at 808 nm (table 2), indicated that a significant fluence rate could be attained in the SNpc by this light delivery route, although the efficiency compared to illumination via the S.S. was smaller by more than one order of magnitude (table 3). Absolute values became even smaller when applying light at 671 nm, close to what was used during the dental treatment. The fraction of fluence rate in the SNpc by shining light only on GB #20, i.e. without an FD1 in the oral cavity, was $\sim 10^{-4}$ mW cm^{-2} at 808 nm and even lower at 671 nm.

In MPTP-treated mice it was shown that a fluence rate of 1–15 mW cm^{-2} within the SNpc is needed to increase the number of dopaminergic cells (Angell-Petersen *et al* 2007). Although the fluence rate in the human SNpc delivered by the oral cavity was one order of magnitude lower, the results indicate that a combination of PBM via the S.S. and oral cavity could be

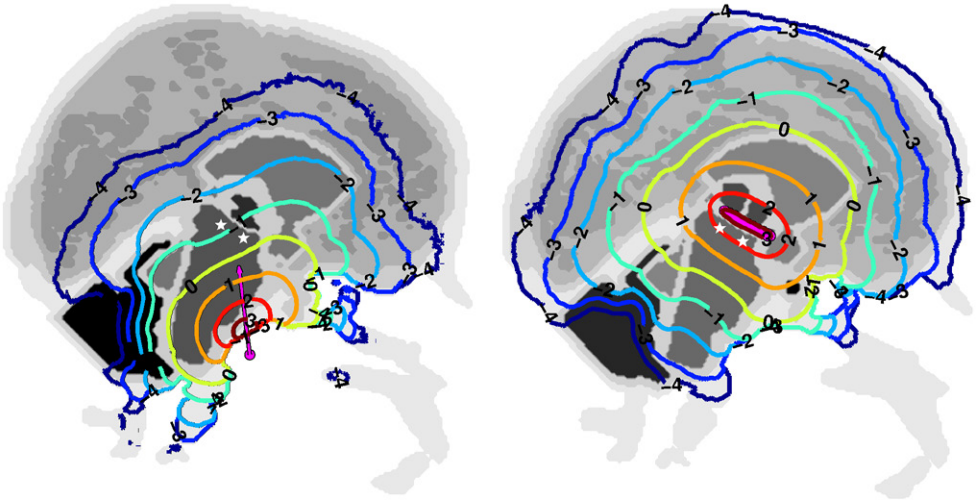

(a) (b)

Figure 6. Figures 6(*a*) and (*b*) show, respectively, the illumination of the SNpc (anterior/posterior location as white asterisks) by an FD1 (magenta arrow) in the oral cavity and a cylindrical diffuser (magenta line) in the third ventricle. Colored contour lines represent the $\log_{10}$ fluence rate computed from the optimized set of optical tissue coefficients at 808 nm. The tissue irradiance by each of the light sources was normalized to 1 W cm^{-2}, i.e. at the surface tissue—light cone or tissue—cylindrical light diffuser. (*a*) Fluence rate distribution at 808 nm for an FD1 (34.7 degree full aperture angle) in the oral cavity. (*b*) Fluence rate distribution at 808 nm for a cylindrical light diffuser (20 mm length and 1 mm diameter) inserted in the third ventricle.

Table 3. The average fluence rate in the SNpc is given for the different light delivery routes and wavelengths.

	Average fluence rate in the SNpc (mW cm^{-2})	
Light delivery route	671 nm	808 nm
Third ventricle	40	95
Sphenoidal sinus	0.3	3.6
Oral cavity	5×10^{-3}	0.2

Note: Absolute values of fluence rate are computed with the derived cadaver's optical coefficients for a tissue irradiance of 1 W cm^{-2}, i.e. at the surface where the FD1 light cone enters the tissue or the surface of the cylindrical light diffuser.

beneficial. It is conceivable that the tissue irradiance in the oral cavity can be set to a higher level than in the S.S. without provoking hyperthermia due to a better choice of light spot locations and moisture cooling the tissue.

3.3.2. Illumination of the SNpc by a cylindrical light diffuser inserted in the third ventricle. One remedy to the low efficiency of transcranial illumination of the SNpc is the intracranial illumination with a light source inserted in the third ventricle, i.e. in the vicinity of pons and thalamus. Not only is the power load on the tissue located around the light source drastically reduced, but the fluence rate distribution can be chosen to be much more localized around the SNpc in order to minimize possible negative side effects of the light on cellular mechanism

elsewhere. Moro *et al* (2013) are currently undertaking experiments to implant light sources into the third ventricle of monkeys to show if PBM preserves behaviour and midbrain dopaminergic cells from MPTP toxicity.

We chose a cylindrical diffuser of 20 mm length and 1 mm diameter as light source to be placed into the ventricle. The diffuser was modeled as a line of 21 equidistant isotropic point sources (Jacques 1998), one every 1 mm. The output power of the cylindrical diffuser was chosen such that the tissue irradiance was 1 W cm^{-2}. It is noteworthy that the simplified brain mesh used for simulation did not contain the third ventricle due to constrains in the voxel size, yet its location could be accurately identified on the original mesh from the MRI.

The fluence rate distribution, shown in figure 6(*b*) for the derived cadaver's optical parameters at 808 nm given in table 2, indicates that a sufficiently high fluence rate can be achieved within the SNpc with a low power output of the source. Comparing the values of fluence rate in table 3 clearly shows the about 20 fold higher efficiency of this light delivery route with respect to any transcranial illumination approach.

4. Conclusions

The objective of the present study was to refine a possible treatment option for PD patients, in a human cadaver model. We wanted to validate the practicalities of light delivery by illuminating the SNpc transcranially and transsphenoidally. We also wanted to validate the light dosimetry by quantifying light distribution within the target brain tissue when illumination takes place from the nasal cavity under endoscopic guidance. To this end, we measured fluence rate distribution in selected intracranial locations while delivering light at two different wavelengths from a location outside the skull and accessible by an endoscope. Our study demonstrates that this approach is possible.

We showed experimentally that the transsphenoidal delivery of light to the relevant target structures of the brain is possible. Our measurements allowed us to validate the model by directly measuring the fluence rate within the target brain structures and to experimentally determine the optical parameters of the brain tissues in this specimen. These will add to an existing body of data and we hope they will be useful to refine published parameters that are notoriously subject to large variations due to experimental conditions or to the specifics of a given specimen. Finally, our study allowed us to determine the light dose delivered to the deep brain for different application routes, a result that could open a number of therapeutic options for PD patients as well as for sufferers of other cerebral disease necessitating light therapy delivered in a non-invasive way.

Acknowledgments

This work was supported in part by the CTI projects 13758.1 and 14660.1, the Swiss National Science Foundation, project 205320_147141/1 and the J Jacobi grant.

The authors wish to thank Drs H Lewine and J Blue for anatomical and instrumentation guidance and J Petersen, head of the cadaver lab facility at Acclarent (MenloPark, CA), for providing any relevant help during the measurement campaign. We would also like to thank the Brainlab staff P Patel and N Wright for the on-site support and F Vollmer and I Thiemann for data preparation and analysis. The present work benefited from the input of Professor H van den Bergh, who provided valuable comments to the writing and undertaking of the research summarized here.

References

Angell-Petersen E, Hirschberg H and Madsen S J 2007 Determination of fluence rate and temperature distributions in the rat brain; implications for photodynamic therapy *J. Biomed. Opt.* **12** 014003

Bays R, Wagnières G, Robert D, Braichotte D, Savary J F, Monnier P and Van Bergh H 1997 Light dosimetry for photodynamic therapy in the esophagus *Lasers Surg. Med.* **20** 290–303

Bevilacqua F, Piguet D, Marquet P, Gross J D, Tromberg B J and Depeursinge C 1999 *In vivo* local determination of tissue optical properties: applications to human brain *Appl. Opt.* **38** 4939–50

Burchman M A 2011 Using photobiomodulation on a severe Parkinson's patient to enable extractions, root canal treatment and partial denture fabrication *J. Laser Dent.* **19** 297–300

Cassidy J, Lilge L and Betz V 2013 Fullmonte: a framework for high-performance Monte Carlo simulation of light through turbid media with complex geometry *Proc. SPIE* **8592** 85920H

Custo A, Wells W M, Barnett A H, Hillman E M and Boas D A 2006 Effective scattering coefficient of the cerebral spinal fluid in adult head models for diffuse optical imaging *Appl. Opt.* **45** 4747–55

Damier P, Hirsch E, Agid Y and Graybiel A 1999 The substantia nigra of the human brain: II. Patterns of loss of dopamine-containing neurons in Parkinson's disease *Brain* **122** 1437–48

Davie C 2008 A review of Parkinson's disease *Br. Med. Bull.* **86** 109–27

De Taboada L, Yu J, El-Amouri S, Gattoni-Celli S, Richieri S, McCarthy T, Streeter J and Kindy M 2011 Transcranial laser therapy attenuates amyloid-beta peptide neuropathology in amyloid-beta protein precursor transgenic mice *J. Alzheimers Dis.* **23** 521–35

Fang Q and Boas D A 2009a Monte carlo simulation of photon migration in 3d turbid media accelerated by graphics processing units *Opt. Express* **17** 20178–90

Fang Q and Boas D A 2009b Tetrahedral mesh generation from volumetric binary and gray-scale images *Proc. 6. IEEE Int. Conf. Symp. Biomed. Imag.: From Nano to Macro* pp 1142–5

Fang Q 2010 Mesh-based Monte Carlo method using fast raytracing in Plücker coordinates *Biomed. Opt. Express* **1** 165–75

Firbank M, Hiraoka M, Essenpreis M and Delpy D T 1993 Measurement of the optical properties of the skull in the wavelength range 650–950 nm *Phys. Med. Biol.* **38** 503–10

Hamblin M and Demidova T 2006 Mechanisms of low level light therapy *Proc. SPIE* vol 6140

Henyey L G and Greenstein J L 1941 Diffuse radiation in the Galaxy *Astrophys. J.* **93** 70–83

Ishimaru A 1978 *Wave Propagation and Scattering in Random Media* (New York: Academic)

Jacques S L 1998 Light distributions from point, line and plane sources for photochemical reactions and fluorescence in turbid biological tissues *Photochem. Photobiol.* **67** 23–32

Karu T 1999 Primary and secondary mechanisms of action of visible to near-IR radiation on cells *J. Photochem. Photobiol. B: Biol.* **49** 1–7

Kordower J, Chu Y, Hauser R, Freeman T and Olanow C 2008 Lewy body-like pathology in long-term embryonic nigral transplants in Parkinson's disease *Nat. Med.* **14** 504–6

Koyama T, Iwasaki A, Ogoshi Y and Okada E 2005 Practical and adequate approach to modeling light propagation in an adult head with low-scattering regions by use of diffusion theory *Appl. Opt.* **44** 2094–103

Lapchak P A and Taboada L D 2010 Transcranial near infrared laser treatment (NILT) increases cortical adenosine-5'-triphosphate (ATP) content following embolic strokes in rabbits *Brain Res.* **1306** 100–5

Lapchak P 2012 Transcranial near-infrared laser therapy applied to promote clinical recovery in acute and chronic neurodegenerative diseases *Exp. Rev. Med. Dev.* **9** 71–83

Lees A J, Hardy J and Revesz T 2009 Parkinson's disease *Lancet* **373** 2055–66

McNaught K and Jenner P 2001 Proteasomal function is impaired in substantia nigra in Parkinson's disease *Neurosci. Lett.* **297** 191–4

Morais V A and De Strooper B 2010 Mitochondria dysfunction and neurodegenerative disorders: cause or consequence *J. Alzheimers Dis.* **20** S255–63

Moro C, Torres N, El Massri N, Ratel D, Johnstone D, Stone J, Mitrofanis J and Benabid A L 2013 Photobiomodulation preserves behaviour and midbrain dopaminergic cells from MPTP toxicity: evidence from two mouse strains *BMC Neurosci.* **14** 219–42

Pitzschke A, Lovisa B, Seydoux O, Haenggi M, Oertel M F, Zellweger M, Tardy Y and Wagnières G 2015 Optical properties of rabbit brain in the red and nir: changes observed under *in-vivo*, post-mortem, frozen and formalin-fixated conditions *J. Biomed. Opt.* **20** 025006

Roggan A 1997 *Dosimetrie Thermischer Laseranwendungen in der Medizin* 16 (ecomed)

Roggan A, Schädel D, Netz U, Ritz J P, Germer C T and Müller G 1999 Effect of preparation technique on the optical parameters of biological tissue *Appl. Phys. B: Lasers Opt.* **69** 445–53

Salomatina E and Yaroslavsky A 2008 Evaluation of the *in vivo* and *ex vivo* optical properties in a mouse ear model *Phys. Med. Biol.* **53** 2797–807

Samii A, Nutt J G and Ransom B R 2004 Parkinson's disease *Lancet* **363** 1783–93

Sharma S K, Kharkwal G B, Sajo M, Huang Y Y, De Taboada L, McCarthy T and Hamblin M R 2011 Dose response effects of 810 nm laser light on mouse primary cortical neurons *Lasers Surg. Med.* **43** 851–9

Shaw V E, Peoples C, Spana S, Ashkan K, Benabid A L, Stone J, Baker G E and Mitrofanis J 2012 Patterns of cell activity in the subthalamic region associated with the neuroprotective action of near-infrared light treatment in mptp-treated mice *Park. Dis.* **2012** 296875

Shaw V E, Spana S, Ashkan K, Benabid A L, Stone J, Baker G E and Mitrofanis J 2010 Neuroprotection of midbrain dopaminergic cells in mptp-treated mice after near-infrared light treatment *J. Comp. Neurol.* **518** 25–40

Temel Y, Kessels A, Tan S, Topdag A, Boon P and Visser-Vandewalle V 2006 Behavioural changes after bilateral subthalamic stimulation in advanced Parkinson disease: a systematic review *Park. Rel. Disord.* **12** 265–72

Trimmer P A, Schwartz K M, Borland M K, De Taboada L, Streeter J and Oron U 2009 Reduced axonal transport in Parkinson's disease cybrid neurites is restored by light therapy *Mol. Neurodeg.* **4** 26

Tromberg B J, Svaasand L O, Fehr M K, Madsen S J, Wyss P, Sansone B and Tadir Y 1996 A mathematical model for light dosimetry in photodynamic destruction of human endometrium *Phys. Med. Biol.* **41** 223

Tuchin V 2007 *Tissue Optics: Light Scattering Methods and Instruments for Medical Diagnosis* vol PM166, 2nd edn (Bellingham, WA: SPIE Pr. Monograph) doi:10.1117/3.684093

Vos M, Lovisa B, Geens A, Morais V A, Wagnières G, Van Den Bergh H, Ginggen A, De Strooper B, Tardy Y and Verstreken P 2013 Near-Infrared 808 nm light boosts complex IV-dependent respiration and rescues a Parkinson-related pink1 Model *PLoS One* **8** e78562

Wang L, Jacques S L and Zheng L 1995 MCML: Monte Carlo modeling of light transport in multi-layered tissues *Comput Methods Programs Biomed.* **47** 131–46

Wang L and Wu H 2007 *Biomedical Optics: Principles and Imaging* (New York: Wiley)

www.AcupunctureProducts.com 2007 Atlas of acupuncture points: point locations

Yaroslavsky A N, Schulze P C, Yaroslavsky I V, Schober R, Ulrich F and Schwarzmaier H J 2002 Optical properties of selected native and coagulated human brain tissues in vitro in the visible and near infrared spectral range *Phys. Med. Biol.* **47** 2059–73

Zhu C and Liu Q 2013 Review of Monte Carlo modeling of light transport in tissues *J. Biomed. Opt.* **18** 050902